

Interplay between topology and localization on superconducting circuits

Xin Guan(关欣), Bingyan Huo(霍炳燕), Gang Chen(陈刚)

Citation: Chin. Phys. B, 2024, 33 (**6**): 060311. DOI: 10.1088/1674-1056/ad342c
Journal homepage: http://cpb.iphy.ac.cn; http://iopscience.iop.org/cpb

What follows is a list of articles you may be interested in

Progress and realization platforms of dynamic topological photonics

Qiu-Chen Yan(闫秋辰), Rui Ma(马睿), Xiao-Yong Hu(胡小永), and Qi-Huang Gong(龚旗煌)
Chin. Phys. B, 2024, 33 (**1**): 010301. DOI: 10.1088/1674-1056/acf284

Exact solution of slow quench dynamics and nonadiabatic characterization of topological phases

Rui Wu(邬睿), Panpan Fang(房盼攀), Chen Sun(孙辰), and Fuxiang Li(李福祥)
Chin. Phys. B, 2023, 32 (**8**): 080304. DOI: 10.1088/1674-1056/acd0a5

Hall conductance of a non-Hermitian two-band system with *k*-dependent decay rates

Junjie Wang(王俊杰), Fude Li(李福德), and Xuexi Yi(衣学喜)
Chin. Phys. B, 2023, 32 (**2**): 020305. DOI: 10.1088/1674-1056/ac9046

Topological superconductivity in Janus monolayer transition metal dichalcogenides

Xian-Dong Li(李现东), Zuo-Dong Yu(余作东), Wei-Peng Chen(陈伟鹏), and Chang-De Gong(龚昌德)
Chin. Phys. B, 2022, 31 (**11**): 110304. DOI: 10.1088/1674-1056/ac8739

Topology of a parity-time symmetric non-Hermitian rhombic lattice

Shumai Zhang(张舒迈), Liang Jin(金亮), and Zhi Song(宋智)
Chin. Phys. B, 2022, 31 (**1**): 010312. DOI: 10.1088/1674-1056/ac364a

---

Interplay between topology and localization on superconducting circuits

Xin Guan(关欣)[1,†], Bingyan Huo(霍炳燕)[1], and Gang Chen(陈刚)[2,3,4]

[1] *Department of Materials and Chemical Engineering, Taiyuan University, Taiyuan* 030032, *China*
[2] *State Key Laboratory of Quantum Optics and Quantum Optics Devices, Institute of Laser Spectroscopy, Shanxi University, Taiyuan* 030006, *China*
[3] *Collaborative Innovation Center of Extreme Optics, Shanxi University, Taiyuan* 030006, *China*
[4] *School of Physics, Zhengzhou University, Zhengzhou* 450001, *China*

(Received 22 December 2023; revised manuscript received 9 March 2024; accepted manuscript online 15 March 2024)

Topological insulators occupy a prominent position in the realm of condensed matter physics. Nevertheless, the presence of strong disorder has the potential to disrupt the integrity of topological states, leading to the localization of all states. This study delves into the intricate interplay between topology and localization within the one-dimensional Su–Schrieffer–Heeger (SSH) model, which incorporates controllable off-diagonal quasi-periodic modulations on superconducting circuits. Through the application of external alternating current (ac) magnetic fluxes, each transmon undergoes controlled driving, enabling independent tuning of all coupling strengths. Within a framework of this model, we construct comprehensive phase diagrams delineating regions characterized by extended topologically nontrivial states, critical localization, and coexisting topological and critical localization phases. The paper also addresses the dynamics of qubit excitations, elucidating distinct quantum state transfers resulting from the intricate interplay between topology and localization. Additionally, we propose a method for detecting diverse quantum phases utilizing existing experimental setups.

Keywords: topology, localization, superconducting circuits

PACS: 03.67.Ac, 73.43.–f, 85.25.Cp, 71.10.–w **DOI:** 10.1088/1674-1056/ad342c

1. Introduction

The recent groundbreaking advancements in superconducting circuits have ushered in a promising era for quantum computing,[1,2] quantum information processing,[3,4] and quantum simulation.[5–7] The flexibility inherent in fabricating superconducting circuits into diverse lattice structures enables the simulation of a broad spectrum of condensed matter phenomena. Examples include spin clusters,[8] topological semimetals,[9,10] quantum walks,[2,11] quantum phase transitions,[12,13] and dynamics associated with many-body quenching.[6] A notable experiment has achieved the precise engineering of a chain of qubits on superconducting circuits, featuring tunable couplings facilitated by external drivings.[14] Utilizing this experimental setup, an in-depth investigation successfully observed the emergence of a topological magnon insulator and accurately determined its winding number.[15] These experiments represent a pioneering approach to exploring exotic topological properties, showcasing the potential of superconducting circuits in advancing our understanding of quantum phenomena.

On the other hand, topological insulators (TIs)[16–25] have garnered significant attention in recent decades. Well-established in the literature, TIs not only feature a bulk gap but also exhibit symmetry-protected gapless states localized at their boundaries. The topological properties of TIs are robust against weak disorders, including fluctuations, imperfections in device fabrications, and environmental noises. This robust property has led to widespread application of TIs in quantum computation and information processing. However, when confronted with sufficiently strong disorder, the integrity of the topological state is disrupted, giving way to a localization state. Furthermore, moderate levels of disorder can induce the topological Anderson insulator.[26–31] Exploring the interplay between topology and localization yields intriguing insights. Quasi-periodic disorder and dimer lattice structures have emerged as noteworthy avenues for inducing localization and topological states, respectively. The renowned Aubry-André (AA)[32–35] and Su–Schrieffer–Heeger (SSH)[36–42] models have been successfully implemented in superconducting circuits.[34,41] Consequently, the appeal lies in the design of a qubit chain featuring staggered coupling strengths and controllable off-diagonal quasi-periodic modulations.

In this paper, we propose a practical approach to realize a one-dimensional SSH model on superconducting circuits with controllable off-diagonal quasi-periodic modulations. Specifically, each transmon is driven by an external ac magnetic flux via the flux-bias line. All parameters can be independently adjusted by manipulating the amplitudes and frequencies of the drivings without increasing circuits complexity. Based on this method, high-fidelity quantum state transfer[14] and topological state detection[15] have been realized in experiments. Through this generalized SSH model,

†Corresponding author. E-mail: guanxin810712@163.com
© 2024 Chinese Physical Society and IOP Publishing Ltd

we have discovered extended topologically nontrivial, critical localization, and co-existing topological and critical localization phases transitions. We utilize the winding number and inverse participation ratio (IPR) to characterize the topological and localization properties, respectively. Additionally, we discuss the dynamics of qubit excitations in this paper. We observe different quantum state transfers, induced by competition between topology and localization. Finally, we address possible experimental observations of these quantum phases. Herein, we introduce the mean chiral displacement (MCD) as a means to probe the winding number. Our results provide a novel avenue for exploring exotic quantum phases and dynamic behaviors arising from the interplay between dimerization and quasi-periodic disorder strengths on superconducting circuits.

2. Model and Hamiltonian

The approach for realizing a one-dimensional SSH model with quasi-periodicity in superconducting circuits is shown in Fig. 1(a). We contemplate a chain of transmon qubits that undergo capacitive coupling with their next-nearest neighbor qubits, as shown in Fig. 1(b). The corresponding Lagrangian is written as

$$\mathcal{L}=\sum_j\left[\frac{C_j}{2}\dot{\phi}_j^2+E_j^{J0}\cos\left(\frac{\phi_j}{\phi_0}\right)\right]+\sum_{\langle i,j\rangle}\left[\frac{C_{ij}}{2}\left(\dot{\phi}_i-\dot{\phi}_j\right)^2\right]. \quad (1)$$

Here, C_j and E_j^{J0} represent the effective capacitance and the Josephson energy of the j-th transmon qubit, respectively. C_{ij} denotes the capacitor used to couple the i-th and j-th transmon qubits. ϕ_j refers to the nodal flux expressed in units of reduced flux quantum $\phi_0=1/(2e)$. The symbol $\langle i,j\rangle$ indicates that the summation runs over all pairs of nearest-neighbor sites. With the canonical coordinate $\hat{\phi}_j$, the canonical momentum $\hat{q}_j=\partial L/\partial\dot{\hat{\phi}}_j$, i.e.,

$$\hat{q}_j=C_j\dot{\hat{\phi}}_j+\sum_{j\langle i\rangle}C_j\left(\dot{\hat{\phi}}_j-\dot{\hat{\phi}}_{j\langle i\rangle}\right), \quad (2)$$

where $j\langle i\rangle$ represents the summation over the nearest-neighbor sites around the j-th site. Taking into account the experimental condition that $C_j\gg\{C_{(j-1)j},C_{j(j+1)}\}$, we approximate the time derivative of the canonical coordinate as $\dot{\hat{\phi}}_j\approx\hat{q}_j/C_j$. Through the application of the Legendre transformation, we derive the corresponding Hamiltonian

$$\hat{H}=\hat{H}_0+\hat{H}_{\rm IJ}, \quad (3)$$

where

$$\hat{H}_0=\sum_j\left(\frac{\hat{q}_j^2}{2\tilde{C}_j}+\frac{\hat{\phi}_j^2}{2L_j^J}-\frac{E_j^{J0}}{24\hat{\phi}_0^4}\hat{\phi}_j^4\right), \quad (4)$$

$$\hat{H}_{\rm IJ}=\sum_{\langle i,j\rangle}\frac{C_{ij}}{C_iC_j}\hat{q}_i\hat{q}_j, \quad (5)$$

with $1/\tilde{C}_j=(C_j-C_{(j-1)j}-C_{j(j+1)})/C_j^2$ and $1/L_j^J=E_j^{J0}/\phi_0^2$.

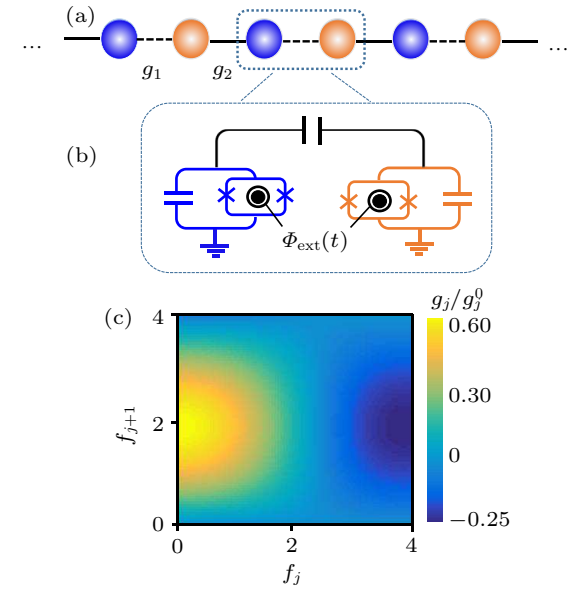


Fig. 1. (a) Schematic diagram of the generalized SSH model with quasi-periodicity. g_1 and g_2 are the coupling strengths. (b) Schematic diagram of transmon qubits chain with tunable coupling strengths. All transmon qubits are coupled with their nearest-neighbor qubits by capacitors. $\Phi_{\rm ext}(t)$ is the external ac magnetic flux. (c) Nearest-neighbor coupling strengths as a function of the parameters f_j and f_{j+1}.

By introducing bosonic annihilation and creation operators

$$\hat{a}_j=\sqrt{\frac{\tilde{C}_j\omega_j^0}{2}}\hat{\phi}_j+{\rm i}\sqrt{\frac{1}{2\tilde{C}_j\omega_j^0}}\hat{q}_j, \quad (6)$$

$$\hat{a}_j^\dagger=\sqrt{\frac{\tilde{C}_j\omega_j^0}{2}}\hat{\phi}_j-{\rm i}\sqrt{\frac{1}{2\tilde{C}_j\omega_j^0}}\hat{q}_j, \quad (7)$$

where $[\hat{a}_j,\hat{a}_{j'}^\dagger]=\delta_{j,j'}$ and $\omega_j^0=\sqrt{8E_j^CE_j^{J0}}$ with $E_j^C=e^2/(2\tilde{C}_j)$, and after applying a rotating-wave approximation, the Hamiltonian (3) is quantized as

$$\hat{H}_0=\sum_j\omega_j^0\hat{a}_j^\dagger\hat{a}_j+\frac{1}{2}V_j\hat{n}_j(\hat{n}_j-1), \quad (8)$$

$$\hat{H}_{\rm IJ}=\sum_j g_j^0\hat{a}_{(j-1)}^\dagger\hat{a}_j+{\rm H.c.}, \quad (9)$$

where H.c. is the Hermitian conjugate, $\hat{n}_j=\hat{a}_j^\dagger\hat{a}_j$ is the particle number operator, and

$$V_j=-E_j^C, \quad (10)$$

$$g_j^0=\frac{C_{(j-1)j}\sqrt{\omega_{(j-1)}^0\omega_j^0}}{2\sqrt{C_{(j-1)}C_j}}. \quad (11)$$

In Eqs. (8) and (9), V_j denotes the anharmonicity of each qubit, g_j^0 is the coupling strength between the j-th and $(j-1)$-th qubits. Given the requirement of $E_j^C\ll E_j^{J0}$ for transmon qubits,[43] we select $E_j^{J0}/E_j^C=50$, $\{C_{(j-1)j},C_{j(j+1)}\}\approx0.5$ fF, and $C_j\approx100$ fF. With these parameters, we derive $V_j/(2\pi)\approx$

200 MHz and $g_j^0/(2\pi) \approx 10$ MHz.[44] This results in a condition that $V_j \gg g_j^0$. In such a case, the qubit exhibits strong anharmonicity, permitting only one boson to be excited per transmon qubit. This implies $V_j\hat{n}_j(\hat{n}_j-1)/2 \equiv 0$, and $\hat{a}_j^\dagger|0\rangle_j = |1\rangle_j$, $\hat{a}_j^\dagger|1\rangle_j = 0$, $\hat{a}_j|0\rangle_j = 0$, and $\hat{a}_j|1\rangle_j = |0\rangle_j$. As a result, the Hamiltonian (3) is expressed as

$$\hat{H} = \sum_j \omega_j^0 \hat{a}_j^\dagger \hat{a}_j + \sum_j \left(g_j \hat{a}_{(j-1)}^\dagger \hat{a}_j + \text{H.c.}\right). \tag{12}$$

The commutation relation can be reformulated as follows:

$$[\hat{a}_j, \hat{a}_{j'}^\dagger] = (1-2\hat{n}_j)\delta_{j,j'}. \tag{13}$$

To achieve tunable coupling strength, an ac microwave driving is applied to each transmon qubit, a procedure experimentally feasible through the flux-bias line.[14] As depicted in Fig. 1(b), we integrate a Josephson junction into a superconducting quantum interference device (SQUID). Given the equal energy of the two Josephson junctions in SQUID, the effective energy is expressed as $E_j^J = 2E_j^{J0}$. Due to the external magnetic flux $\Phi_j(t)$, a phase difference $\Phi_j(t)/\phi_0$ emerges between the two Josephson junctions, leading to a modification in the potential energy of each qubit,

$$\begin{aligned} & E_j^{J0}\left[\cos\left(\frac{\phi_j}{\phi_0} + \frac{\Phi_j(t)}{2\phi_0}\right) + \cos\left(\frac{\phi_j}{\phi_0} - \frac{\Phi_j(t)}{2\phi_0}\right)\right] \\ = \; & E_j^J(t)\cos\left(\frac{\phi_j}{\phi_0}\right). \end{aligned} \tag{14}$$

In this equation, $E_j^J(t) = E_j^J\cos[\Phi_j(t)/2\phi_0]$. The frequency of the j-th qubit is given by

$$\omega_j(t) = \omega_j^0\sqrt{\cos[\Phi_j(t)/2\phi_0]}.$$

Here we designate the external magnetic flux as

$$\Phi_j(t) = \alpha_j\cos(u_j^0 t + \phi_j^0), \tag{15}$$

where $\alpha_j \ll \omega_j^0$, u_j^0, and ϕ_j^0 represent the amplitude, frequency, and phase of the external magnetic flux, respectively. Subsequently, we perform a Taylor expansion of the frequency $\omega_j(t)$ at $\Phi_j(t) = 0$,

$$\omega_j(t) \approx \omega_j^0 + \varepsilon_j\sin(u_j t + \phi_j), \tag{16}$$

where $\varepsilon_j = \omega_j^0\alpha_j^2/(4\phi_0^2)$, $u_j = 2u_j^0$, and $\phi_j = 2\phi_j^0 + 3\pi/2$. In experiments,[14] u_j is of the order ~ 100 MHz, which is significantly larger than g_j^0. Then a unitary operator $\hat{U} = \hat{U}_\text{A} \times \hat{U}_\text{B}$ is introduced to transform Hamiltonian (12) with the frequency $\omega_j(t)$, where

$$\begin{aligned} \hat{U}_\text{A} &= \exp\left[-\text{i}\sum_{j=1}^N \omega_j^0 \hat{n}_j t\right], \\ \hat{U}_\text{B} &= \exp\left[\text{i}\sum_{j=1}^N f_j\cos(u_j t + \phi_j)\right], \end{aligned} \tag{17}$$

with $f_j = \varepsilon_j/u_j$ and N is the number of qubits. The transformed Hamiltonian can be derived as

$$\begin{aligned} \hat{H}_t &= \hat{U}^\dagger\hat{H}\hat{U} + \text{i}\frac{\text{d}\hat{U}^\dagger}{\text{d}t}\hat{U} \\ &= \sum_{j=1}^{N-1} g_j^0\{\text{e}^{-\text{i}\Delta_j t}\exp[-\text{i}f_j\cos(u_j t + \phi_j)] \\ &\quad \times \exp[\text{i}f_{j+1}\cos(u_{j+1}t + \phi_{j+1})]\hat{a}_j^\dagger\hat{a}_{j+1} + \text{H.c.}\}, \end{aligned} \tag{18}$$

where $\Delta_j = \omega_{j+1}^0 - \omega_j^0$. We select $\Delta_j = u_{j+1}(-u_{j+1})$ for odd (even) j. Subsequently, we employ the Jacobi–Anger identity

$$\exp[\text{i}f_j\cos(u_j t + \phi_j)] = \sum_{-\infty}^{\infty} \text{i}^m \text{J}_m(f_j)\exp[\text{i}m(u_j t + \phi_j)],$$

and apply the rotating-wave approximation to the Hamiltonian in Eq. (18). Here $\text{J}_m(f_j)$ represents the m-th Bessel function of the first kind. By neglecting the oscillating terms and setting $\phi_j = -\pi(0)$ for odd (even) j, we can derive

$$\hat{H}_\text{eff} = \sum_{j=1}^{N-1} g_j\left(\hat{a}_j^\dagger\hat{a}_{j+1} + \text{H.c.}\right), \tag{19}$$

where the coupling strength is

$$g_j = g_j^0\text{J}_0(f_j)\text{J}_1(f_{j+1}). \tag{20}$$

As evident, the coupling strength g_j can be tuned from $-0.25g_j^0$ to $0.6g_j^0$ by changing the parameters f_j and f_{j+1} as shown in Fig 1(c). Therefore the ratio between the two coupling strengths g_j/g_{j+1} can be tuned to arbitrary values. To achieve the SSH model with controllable off-diagonal quasi-periodic modulations, we set $g_j = g[1+\lambda+\delta\cos(2\pi\beta j)]$ for odd j and $g_j = g[1-\lambda+\delta\cos(2\pi\beta j)]$ for even j. The parameter $\beta = (\sqrt{5}-1)/2$. λ and δ indicate the dimerization and quasi-periodic disorder strengths respectively. In this paper we choose $g = 1$ as the energy unit. In the subsequent discussion, we denote the creation (annihilation) operators of qubits with odd and even j as $\hat{a}_i^\dagger$ ($\hat{a}_i$) and $\hat{b}_i^\dagger$ ($\hat{b}_i$), respectively, where i is the unit cell index in the case of $\delta = 0$. We consider the single excitation throughout our work.

3. Phase diagram and quantum state transfer

3.1. Phase diagram

In this section, we focus on elucidating the phase diagram arising from the interplay between quasi-periodic disorder and dimerization strengths. We utilize a set of 50 transmon qubits in our investigation.

When the disorder is absent in the generalized SSH model (19), it reduces to the SSH model. The energy bands of the SSH model are illustrated in Fig. 2(a1), revealing the existence of degenerate zero-energy modes persisting within the middle of the energy gap, characterized by a positive value

of λ. The corresponding wave functions exhibit exponential localization at the boundaries of the system, as depicted in Fig. 2(a2). Upon activating disorder, we present the evolution of these energy bands in Figs. 2(b1) and 2(c1). This illustrates that with increasing δ, the energy gap near zero-energy vanishes within the small λ region.

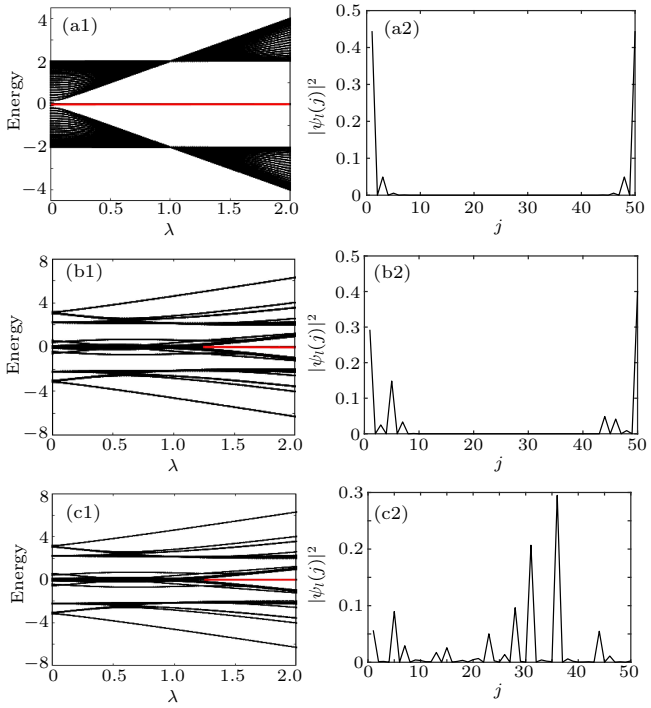


Fig. 2. Energy bands and wave functions of the $N/2$-th and $(N/2+1)$-th $[l = N/2, (N/2+1)]$ eigenstates for the Hamiltonian in Eq. (19) with open boundary condition. (a1)–(c1) Energy bands as functions of λ with (a1) $\delta = 0$, (b1) $\delta = 1$, and (c1) $\delta = 2$. (a2)–(c2) Wave functions with (a2) $\delta = 0$ and $\lambda = 0.5$, (b2) $\delta = 1$ and $\lambda = 0.5$ and (c2) $\delta = 2$ and $\lambda = 0.5$.

Figures 2(a2)–2(c2) demonstrate the transition of edge states into bulk of the system as δ increases. These findings highlight that strong disorder can only destroy topological states when λ is small. This suggests that the interplay between dimerization strength λ and quasi-periodic disorder strength δ induces a transition from a topologically trivial to a nontrivial phase. In the subsequent, we will provide an analytical explanation for these results.

With $\delta = 0$, we can ansatz the edge states as

$$|\Psi\rangle_{E=0} = \sum_i (\rho_1^i w_1 \hat{a}_i^\dagger \pm \rho_2^i w_2 \hat{b}_i^\dagger)\,|G\rangle\,,$$

where $|G\rangle$ represents the vacuum state. According to the Schrödinger equation, $\hat{H}\,|\Psi\rangle_{E=0} = 0$, i.e.,

$$(g_1\rho_2^i + g_2\rho_2^{i-1})w_2\hat{a}_i^\dagger\,|G\rangle + (g_2\rho_1^{i+1} + g_1\rho_1^i)w_1\hat{b}_i^\dagger\,|G\rangle = 0, \quad (21)$$

the edge states can be obtained as

$$|\Psi\rangle_{E=0} = \sum_i \left[\left(-\frac{g_1}{g_2}\right)^i w_1\hat{a}_i^\dagger \pm \left(-\frac{g_2}{g_1}\right)^i w_2\hat{b}_i^\dagger\right]|G\rangle\,. \quad (22)$$

These results indicate that the state is localized in proximity to the leftmost ($i = 1$) a-type site and rightmost ($i = N/2$) b-type site.

Next, we introduce disorder and observe the variations in ρ_1 and ρ_2,

$$\rho_1 = -\frac{1-\lambda+\delta\cos[2\pi\beta\,(2\mathrm{i}-1)]}{1+\lambda+\delta\cos[2\pi\beta\,(2\mathrm{i})]}, \quad (23)$$

$$\rho_2 = -\frac{1+\lambda+\delta\cos[2\pi\beta\,(2\mathrm{i})]}{1-\lambda+\delta\cos[2\pi\beta\,(2\mathrm{i}-1)]}, \quad (24)$$

which depend on the qubits' indexes. Equations (23) and (24) indicate that the presence of non-zero δ prevents ρ_1 and ρ_2 from consistently being larger or smaller than 1. This implies that the behavior of topological edge states is influenced by δ. To characterize distinct topological phases in the case of $\delta \neq 0$, we compute the topological invariant. Since the Hamiltonian (19) possesses chiral, time-reversal, and particle–hole symmetries, it belongs to class BDI of the Altland–Zirnbauer classification. The topological properties of the system can be characterized by the winding number, which can be easily calculated in momentum space for translationally invariant systems. However, in the presence of non-zero disorder strength, translational symmetry is broken, and thus the computation of winding number must be performed in real space using a local quantity,[30,45]

$$\nu = \frac{1}{2}\mathrm{Tr}'(\hat{P}\hat{\Gamma}\hat{X}\hat{P}), \quad (25)$$

where Tr′ indicates the trace over the single unit cell in the middle of the qubit chian. $\hat{P} = \hat{P}_+ - \hat{P}_-$ with $\hat{P}_+$ ($\hat{P}_-$) being the projection operator of the eigenstates with positive (negative) eigenenergies. $\hat{\Gamma} = \sum_{i=1}^{N}\left(\hat{\Gamma}_{a_i}^{\mathrm{e}} - \hat{\Gamma}_{b_i}^{\mathrm{e}}\right)$ where $\hat{\Gamma}_{di}^{\mathrm{e}} = |e\rangle_{di}\langle e|$ with $|e\rangle_{di}$ $(d = a, b)$ indicates the state with exciting the d-type qubit at the i-th unit cell. $\hat{X}$ is the unit-cell position operator. We numerically calculate the winding number and show the topological nontrivial and trivial phases in regions I + II ($\delta < 1+\lambda$) and III ($\delta > 1+\lambda$) of Fig. 3(a), respectively. Furthermore we show the winding number changes from region I + II to III in Fig. 3(b). We find the winding number ν suddenly approaches 0 from 1 as the system enters III. This indicates that the system goes from topologically trivial to nontrivial phases. This finding accurately demonstrates that the coexistence of strong disorder and weak dimerization strengths can result in the annihilation of topological states.

On the other hand, localization always emerges in a quasi-periodic system. We can capture the localization property of the n-th eigenstate $|\Psi_n\rangle = \sum_j \psi_n(j)\,|e\rangle_j$ ($\psi_n(j)$ is the wave function) in our system by the inverse participation ratio (IPR), defined as $\mathrm{IPR}_n = \sum_j |\psi_n(j)|^4$. For an extended (a fully localized) state, $\mathrm{IPR}_n \approx (2N)^{-1}$ ($\mathrm{IPR}_n \approx 1$). For a critically localized state,[46–49] $\mathrm{IPR}_n \approx (2N)^{-\theta}$, where $\theta \in (0,1)$ depends on the multifractal nature of the wave function. We present the phase diagram in Fig. 3(a) and find our system exhibits localization transition boundaries, where the values of IPR_n shift

from zero in region I ($\delta < 1-\lambda \cup \delta < \lambda - 1$) to finite values between 0 and 1 in regions II + III ($\delta > 1-\lambda \cap \delta > \lambda - 1$). This abrupt changing of IPR$_n$ is shown in Fig. 3(c), which depicts the energy bands with open boundary conditions marked by the values of IPR$_n$. This result suggests that the localization properties are also influenced by the strength of dimerization.

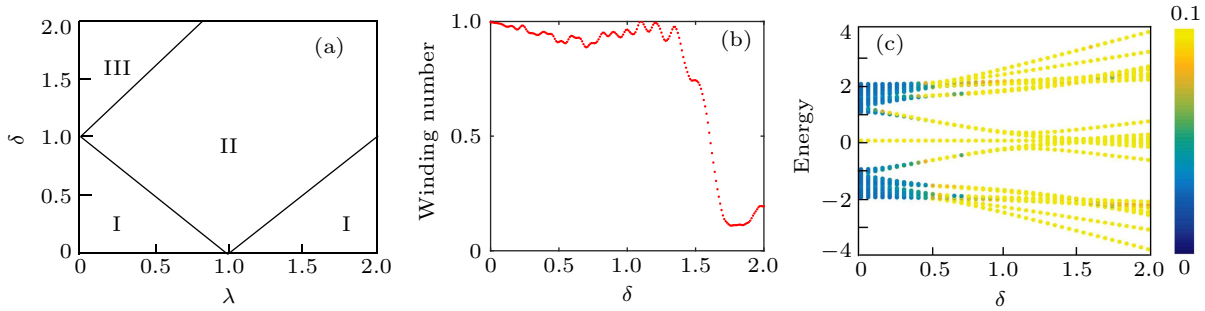


Fig. 3. (a) Phase diagram in the λ–δ plane. I is extended topologically nontrivial phase with winding number $\nu = 1$. II is the coexisting topological critical localization phase with winding number $\nu = 1$. III is the critical localization phase with winding number $\nu \approx 0$. (b) Winding number as a function of δ with $\lambda = 0.5$. (c) Energy bands denoted by the values of IPR$_n$ as a function of δ with $\lambda = 0.5$.

In conclusion, the interplay between δ and λ give rise to three distinct quantum phases: extended topologically nontrivial [region I in Fig. 3(a)], coexisting topological and critical localization [region II in Fig. 3(a)], and critical localization [region III in Fig. 3(a)] phases. Furthermore, figure 3(c) indicates the absence of mobility edges except for a few edge states.

3.2. Quantum state transfer

In this section, we illustrate the transfer of quantum states both in the presence and absence of quasi-periodic disorder.

In this context, we initially examine the scenario with $\delta = 0$, where the edge states are expressed in Eq. (22). In the instance of an even number of qubits, these edge states localize at both boundaries of the system. Consequently, irrespective of the variations in λ, the quantum state localized at the leftmost boundary cannot transfer to the rightmost. Conversely, in the case of an odd number of qubits, both boundaries consist of a-type qubits, resulting in edge states localizing at the left- and rightmost boundaries for $\lambda > 0$ and $\lambda < 0$, respectively. This implies that quantum state transfer can occur as λ changes from negative to positive values. To achieve this change, we set $\lambda = \cos(\gamma)$ with $\gamma \in [0, \pi]$. To validate this quantum state transfer, the periodic parameter γ is considered as a function of time, denoted as $\gamma = \Omega t$ with Ω representing the rate of change. The quantum state transfer process is required adiabatic. Therefore Ω needs to be sufficiently small. We present the fidelity of this quantum state transfer with different Ω in Fig. 4(a). The initial state is chosen as the leftmost edge state, expressed as $|L\rangle = |egg...g\rangle$. The fidelity is denoted as $F = \langle R|\psi_f\rangle$, where $|R\rangle = |gg..ge\rangle$ represents the rightmost edge state and $|\psi_f\rangle$ is the final state. We find the fidelity can persist as 1 with $\log_{10}\Omega < -1.5$. This implies the final evolved state is the ideal state with $\Omega < 10^{-1.5}$. In the following discussion we choose $\Omega = 0.01$. The temporal evolution of the qubits' excitations is illustrated in Fig. 4(b). This result demonstrates that the quantum state is effectively transferred from the leftmost boundary to the rightmost boundary of the system through bulk as γ varying from 0 to π.

Subsequently, the effect of disorder strength δ on the quantum state transfer is discussed. During the quantum state transfer process, λ changes from 1 to -1 with time increasing. When t increases to about $0.5\pi/\Omega$, $\lambda \approx 0$. At this point, compared with λ, non-zero δ is dominant for the quantum state transfer. This may induce the final evolved state far away from the ideal right-most edge state. Then, we present the variation of the fidelity F with δ increasing in Fig. 4(c). As δ remains sufficiently small, the quantum state transfer persists. However, as δ surpasses a certain threshold, the transfer becomes unfeasible.

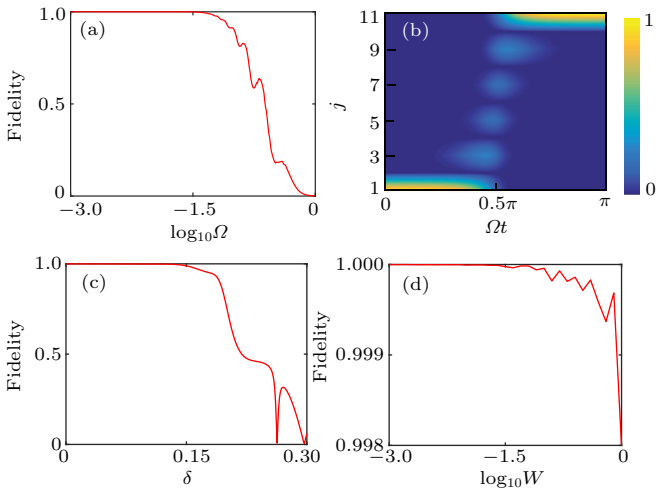


Fig. 4. (a) The fidelity F as a function of $\log_{10}\Omega$ with $\delta = 0$. (b) Time evolution of qubits' excitations with $\delta = 0$. (c) The fidelity F as a function of δ. (d) The fidelity F as a function of $\log_{10}W$. In all figures $\lambda = \cos(\Omega t)$ and number of the qubits is 11.

The noise in practical experiments can influence the quantum state transfer. We consider noise to the coupling coefficients as $g'_j = g_j + W\tau_j$, where W is the noise strength and $\tau \in [-0.5, 0.5]$ is a random number. We show the fidelity F as a function of $\log_{10}W$ in Fig. 4(d). For $\log_{10}W < -1$, a

wide plateau appears at $F = 1$. As $\log_{10} W$ further increasing, we find the fidelity decreases slowly. This phenomenon is a hallmark of the topologically assisted quantum state transfer.

We then investigate the quantum state transfer while varying the strength of quasi-periodic disorder δ. Similarly to the prior discussion, we choose $\delta = \Omega t$ and adopt $|L\rangle$ as the initial state. The temporal evolution of the qubits' excitations is presented in Fig. 5. It is observed that the qubits' excitations localize at the leftmost boundary when Ωt is smaller than approximately 0.5, indicative of the system being in a topologically extended phase, as depicted in Fig. 3(a). As Ωt varies from 0.5 to 1.5, these excitations gradually depart from the leftmost boundary and diffuse throughout the bulk of the system. This scenario corresponds to the system being in a co-existing topological and critical localization phase, as illustrated in Fig. 3(a). Thus, this diffusion arises due to the competition between topology and localization. In the region where $\Omega t > 1.5$, the qubits' excitations are localized at one or some bulk states of the system due to critical localization phase with topologically trivial properties as indicated in Fig. 3(a). These results suggest that the quantum state can transfer from a boundary state to certain states within the bulk, induced by the interplay between topology and localization.

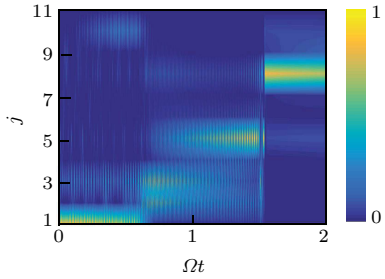


Fig. 5. Time evolution of qubits' excited states with $\lambda = 0.5$ and $\delta = \Omega t$. The number of qubits is 10.

4. Possible experimental observation

In this section, we propose an experimental scheme for detecting the aforementioned phases. Additionally, it is worth noting that the quantum state transfer can be directly observed. In superconducting circuits, the winding number expression (25) can be dynamically detected through the mean chiral displacement (MCD) $\overline{C}$,[30,50,51] where $\overline{C} = \nu/2$. The MCD is defined as follows:

$$\overline{C} = \frac{1}{T}\int_0^T C\,\mathrm{d}t. \tag{26}$$

In this context, the MCD is expressed as $C = \langle\psi(t)|\hat{\Gamma}\hat{X}|\psi(t)\rangle$, where $|\psi(t)\rangle = \mathrm{e}^{-\mathrm{i}\hat{H}t}|\psi(0)\rangle$ represents the state of the system at time t. $|\psi(0)\rangle$ is the initial state. To detect the MCD, we employ four qubits. Initially, we prepare the state $|\psi(0)\rangle = |gegg\rangle$, where one of the middle qubits is excited and the others are in the ground states. The subsequent time evolution of this excitation is directly measured, as depicted in Figs. 6(a)–6(c). In the extended topologically nontrivial [Fig. 6(a)] and co-existing topological and critical localization phases [Fig. 6(b)], the excitations are confined within the bulk, whereas in the topologically trivial phase [Fig. 6(c)], the excitations propagate to the boundaries of the qubit chain. Subsequently, the time evolution of the CD is derived, as depicted in Fig. 6(d). The CD exhibits oscillations around -0.01 and 0.42 in topological trivial and nontrivial phases, respectively, indicating distinct winding numbers of -0.02 and 0.84. This observation is in close proximity to the ideal values.

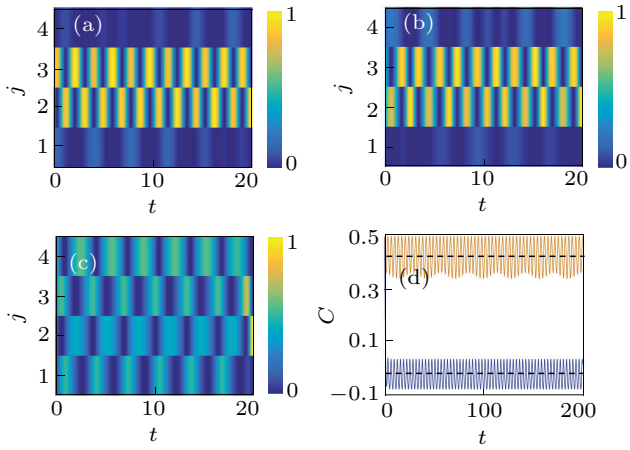


Fig. 6. Time evolution of all qubits' excited states in two-dimensional representation with (a) $\delta = 0.2$, (b) $\delta = 1$, and (c) $\delta = 2$. (d) Time evolution of chiral displacement with $\delta = 2$ and $\delta = 0.2$ denoted by blue and orange curves, respectively. In all figures $\lambda = 0.5$.

To identify critical localization, the determination of IPR_n is essential. IPR_n has been detected in experiments by considering Fourier transform of the experimental datas.[34] Before the detection, an initial state $|\chi\rangle = (|\mathrm{Vac}\rangle + |1_n\rangle)/\sqrt{2}$ needs to be prepared and evolves under the Hamiltonian (19), where $|\mathrm{Vac}\rangle = |0\rangle_1|0\rangle_2\cdots|0\rangle_N$ is the vacuum state and $|1_n\rangle = |0\rangle_1|0\rangle_2\cdots|1\rangle_n\cdots|0\rangle_N$ is a Fock state. According to Schrödinger equation, the state at time t is

$$|\chi(t)\rangle_n = \frac{1}{\sqrt{2}}\left(|\mathrm{Vac}\rangle + \sum_j \psi_{j,n}\,\mathrm{e}^{-\mathrm{i}E_j t}|\Psi\rangle_j\right), \tag{27}$$

where $\psi_{j,n} = \langle\Psi_j|1_n\rangle$ and $|\Psi_j\rangle$ is the eigenstate with eigenenergy E_j. The expectation value of the Pauli matrices σ_n^x and σ_n^y in subspace can be detected directly by applying a microwave $\pi/2$ pulse to the n-th qubit. Then the value of $\zeta(n) = \langle\sigma_n^x\rangle + \mathrm{i}\langle\sigma_n^y\rangle = (\sum_j |\psi_{j,n}|^2\,\mathrm{e}^{-\mathrm{i}E_j t})/2$ can be obtained. $|\psi_{j,n}|^2$ can be measured by reading the magnitude of Fourier transform of $\zeta(n)$. Finally, the IPR_n can be directly derived.

5. Conclusion

In summary, we have presented a feasible experimental method to realize a one-dimensional SSH model with controllable off-diagonal quasi-periodic modulations in superconducting circuits. Achieving independently tunable coupling

strengths involves applying an external ac magnetic flux to drive each transmon qubit. Subsequently, the generalized SSH model, featuring both dimerization and quasi-periodic components, is constructed. Within this framework, we discover phase transitions among extended topologically nontrivial, critical localization, and coexisting topological and critical localization phases. The winding number and inverse participation ratio (IPR) serve as characterization for the topological and localization properties, respectively. Additionally, the dynamics of qubits' excitations are explored, revealing distinctive quantum state transfers resulting from the interplay between topology and localization. Moreover, we propose a method for detecting various quantum phases using existing experimental setups. Notably, the mean chiral displacement (MCD) is introduced as a tool for probing the winding number. These findings offer a new avenue for investigating exotic quantum phases and dynamic behaviors arising from the interplay between dimerization and quasi-periodic disorder strengths in superconducting circuits.

Acknowledgement

Project supported by the Natural Science Foundation of Shanxi Province, China (Grant No. 202103021223010).

References

[1] Buluta I, Ashhab S and Nori F 2011 *Rep. Phys.* **74** 104401

[2] Gong M, Wang S, Zha C, Chen M C, Huang H L, Wu Y, Zhu Q, Zhao Y, Li S, Guo S, Haoran Q, Yangsen Y, Fusheng C, Chong Y, Jiale Y, Daojin F, Dachao W, Hong S, Hui D, Hao R, Kaili Z, Sirui C, Lin J, Xu Y, Sun L, Guo C, Li N, Liang F, Bastidas V M, Kae N, Munro W J, Huo Y H, Lu C Y, Peng C Z, Zhu X and Pan J W 2021 *Science* **372** 948

[3] Wendin G 2017 *Rep. Phys.* **80** 106001

[4] Blais A, Girvin S M and Oliver W D 2020 *Nat. Phys.* **16** 247

[5] Georgescu I M, Ashhab S and Nori F 2014 *Rev. Mod. Phys.* **86** 153

[6] Zhang X, Kim E, Mark D K, Choi S and Painter O 2023 *Science* **379** 278

[7] Ying C, Cheng B, Zhao Y, Huang H L, Zhang Y N, Gong M, Wu Y, Wang S, Liang F, Lin J, Yu X, Hui D, Hao R, Cheng Zh P, Man H Y, Xiao B Z and Pan J W 2023 *Phys. Rev. Lett.* **130** 110601

[8] Wang D W, Song C, Feng W, Cai H, Xu D, Deng H, Li H, Zheng D, Zhu X, Wang H, Zhu S Y and Scully O 2019 *Nat. Phys.* **15** 382

[9] Tan X, Zhang D W, Liu Q, Xue G, Yu H F, Zhu Y Q, Yan H, Zhu S L and Yu Y 2018 *Phys. Rev. Lett.* **120** 130503

[10] Tan X, Zhao Y, Liu Q, Xue G, Yu H F, Wang Z and Yu Y 2019 *Phys. Rev. Lett.* **122** 010501

[11] Yan Z, Zhang Y R, Gong M, Wu Y, Zheng Y, Li S, Wang C, Liang F, Lin J, Xu Y, Guo C, Sun L, Peng Z C, Xia K, Deng H, Rong H, You Q, Nori J F, Fan H, Zhu X and Pan J W 2019 *Science* **364** 753

[12] Kaur K, Sépulcre T, Roch N, Snyman I, Florens S and Bera S 2021 *Phys. Rev. Lett.* **127** 237702

[13] Dborin J, Wimalaweera V, Barratt F, Ostby E, O'Brien T E and Green A G 2022 *Nat. Commun.* **13** 5977

[14] Li X, Ma Y, Han J, Chen T, Xu Y, Cai W, Wang H, Song Y, Xue Z Y, Yin Z Q and Sun L 2018 *Phys. Rev. Appl.* **10** 054009

[15] Cai W, Han J, Mei F, Xu Y, Ma Y, Li X, Wang H, Song Y, Xue Z Y, Yin Z Q, Jia S and Sun L 2019 *Phys. Rev. Lett.* **123** 080501

[16] Hasan M Z and Kane C L 2010 *Rev. Mod. Phys.* **82** 3045

[17] Qi X L and Zhang S C 2011 *Rev. Mod. Phys.* **83** 1057

[18] Khanikaev A B, Mousavi S H, Tse W K, Kargarian M, MacDonald A H and Shvets G 2013 *Nat. Mater.* **12** 233

[19] Rechtsman M C, Zeuner J M, Plotnik Y, Lumer Y, Podolsky D, Dreisow F, Nolte S, Segev M and Szameit A 2013 *Nature* **496** 196

[20] Maciejko J and Fiete G A 2015 *Nat. Phys.* **11** 385

[21] Rachel S 2018 *Rep. Phys.* **81** 116501

[22] Schindler F, Cook A M, Vergniory M G, Wang Z, Parkin S S, Bernevig B A and Neupert T 2018 *Sci. Adv.* **4** eaat0346

[23] Tokura Y, Yasuda K and Tsukazaki A 2019 *Nat. Rev. Phys.* **1** 126

[24] Rudner M S and Lindner N H 2020 *Nat. Rev. Phys.* **2** 229

[25] Biesenthal T, Maczewsky L J, Yang Z, Kremer M, Segev M, Szameit A and Heinrich M 2022 *Science* **376** 1114

[26] Li J, Chu R L, Jain J K and Shen S Q 2009 *Phys. Rev. Lett.* **102** 136806

[27] Groth C, Wimmer M, Akhmerov A, Tworzyd lo J and Beenakker C 2009 *Phys. Rev. Lett.* **103** 196805

[28] Guo H M, Rosenberg G, Refael G and Franz M 2010 *Phys. Rev. Lett.* **105** 216601

[29] Stützer S, Plotnik Y, Lumer Y, Titum P, Lindner N H, Segev M, Rechtsman M C and Szameit A 2018 *Nature* **560** 461

[30] Meier E J, An F A, Dauphin A, Maffei M, Massignan P, Hughes T L and Gadway B 2018 *Science* **362** 929

[31] Zhang W, Zou D, Pei Q, He W, Bao J, Sun H and Zhang X 2011 *Phys. Rev. Lett.* **126** 146802

[32] Sokoloff J 1985 *Phys. Rep.* **126** 189

[33] Thouless D 1988 *Phys. Rev. Lett.* **61** 2141

[34] Roushan P, Neill C, Tangpanitanon J, Bastidas V M, Megrant A, Barends R, Chen Y, Chen Z, Chiaro B, Dunsworth A, Fowler A, Foxen B, Giustina M, Jeffrey E, Kelly J, Lucero E, Mutus J, Neeley M, Quintana C, Sank D, Vainsencher A, Wenner J, White T, Neven H, Angelakis G and Martinis D J 2017 *Science* **358** 1175

[35] An F A, Padavić K, Meier E J, Hegde S, Ganeshan S, Pixley J, Vishveshwara S and Gadway B 2021 *Phys. Rev. Lett.* **126** 040603

[36] Su W, Schrieffer J and Heeger A J 1979 *Phys. Rev. Lett.* **42** 1698

[37] Marchand D, Filippis G D, Cataudella V, Berciu M, Nagaosa N, Prokof'Ev N, Mishchenko A and Stamp P 2010 *Phys. Rev. Lett.* **105** 266605

[38] Meier E J, An F A and Gadway B 2016 *Nat. Commun.* **7** 13986

[39] Xing B, Chiu W T, Poletti D, Scalettar R T and Batrouni G 2021 *Phys. Rev. Lett.* **126** 017601

[40] Kiczynski M, Gorman S, Geng H, Donnelly M, Chung Y, He Y, Keizer J and Simmons M 2022 *Nature* **606** 694

[41] Youssefi A, Kono S, Bancora A, Chegnizadeh M, Pan J, Vovk T and Kippenberg T J 2022 *Nature* **612** 666

[42] Wang Z, Wang X, Hu Z, Bongiovanni D, Jukic D, Tang L, Song D, Morandotti R, Chen Z and Buljan H 2023 *Nat. Phys.* **19** 992

[43] Koch J, Terri M Y, Gambetta J, Houck A A, Schuster D I, Majer J, Blais A, Devoret M H, Girvin S M and Schoelkopf R J 2007 *Phys. Rev. A* **76** 042319

[44] Ye Y, Ge Z Y, Wu Y, Wang S, Gong M, Zhang Y R, Zhu Q, Yang R, Li S, Liang F, Lin J, Xu Y, Guo C, Sun L, Cheng C, Ma N, Meng Z Y, Deng H, Rong H, Lu C Y, Peng C Z, Fan H, Zhu X and Pan J W 2019 *Phys. Rev. Lett.* **123** 050502

[45] Mondragon S I, Hughes T L, Song J and Prodan E 2014 *Phys. Rev. Lett.* **113** 046802

[46] Thouless D J 1983 *Phys. Rev. B* **28** 4272

[47] Chang I, Ikezawa K and Kohmoto M 1997 *Phys. Rev. B* **55** 12971

[48] Liu F, Ghosh S and Chong Y D 2015 *Phys. Rev. B* **91** 014108

[49] Wang Y, Cheng C, Liu X J and Yu D 2021 *Phys. Rev. Lett.* **126** 080602

[50] Meier E J, An F A and Gadway B 2016 *Nat. Commun.* **7** 13986

[51] Cardano F, D'Errico A, Dauphin A, Maffei M, Piccirillo B, Lisio D C, Filippis G D, Cataudella V, Santamato E, Marrucci L, Lewenstein M and Massignan P 2017 *Nat. Commun.* **8** 15516